JURNAL LOCUS: Penelitian & Pengabdian
Volume 5 No. 11 November 2026, pp 10144-10163
E-ISSN 2829-7334
DOI: 10.58344/locus.v5i11.6499

Lagrangian Formulation of Interfacial Energetics and Higher-Order Electric-Field Response in PLA/PCL/PEG–Nanozeolite Membranes

Muhammad Satya Putra Gantada, Agung Mataram*
Universitas Sriwijaya, Indonesia
Email: amataram@unsri.ac.id*

Keywords:
density functional theory; variational principle; electric-field-assisted NIPS; PLA/PCL/PEG; nanozeolite.

This is an open access article under the CC BY-SA license.

Copyright © 2026 by Author. Published by Riviera Publishing

ABSTRACT

Quantum-mechanical descriptions of electrically assisted membrane fabrication require a consistent relationship among the applied electric field, interfacial structure, and electronic energy. This study developed a Lagrangian and variational framework for density functional theory (DFT) modeling of poly(lactic acid)/polycaprolactone/poly(ethylene glycol) (PLA/PCL/PEG)–nanozeolite interfaces relevant to electric-field-assisted nonsolvent-induced phase separation (E-NIPS) under an applied voltage of 10 kV. The formulation integrated a low-energy electromagnetic description with constrained electron-density and orbital stationarity conditions, interfacial interaction energies, and field-induced responses. A contact-dependent analytical potential was constructed by combining a Morse potential with dipolar, quadratic, and fourth-order electric-field contributions. Assuming an electrode separation of 3 cm and a uniform electric field, an applied voltage of 10 kV corresponded to a nominal electric-field strength of 3.333×10^5 V m^{-1}. The combined polymer–zeolite interfacial contact model yielded a minimum interaction energy of −91.30 kJ mol^{-1} and a nominal-field-induced energy shift of −2.8459 J mol^{-1}. Geometric relaxation increased the calculated polarizability from 310.000 to 313.4775 atomic units (a.u.). Central finite-difference calculations demonstrated the expected second-order dependence of truncation error on the electric-field step size, whereas a reduced quadratic energy model yielded a root mean square error (RMSE) of 0.36189 J mol^{-1} across six additional electric-field evaluation points. Compared with the relaxed second-order expansion, the fourth-order formulation reduced the maximum truncation error for the C5 configuration from 0.81463 to 0.001035 J mol^{-1}. The theoretical derivations distinguished structural relaxation effects at the polymer–zeolite interface from biases in the estimated response coefficients arising from the omission of higher-order electric-field terms. The resulting equations established a reproducible representation of interfacial energetics and specified the variational potential required for subsequent density-functional extensions. However, quantitative calibration and independent validation of the proposed framework require atomistic DFT reference calculations of electronic energies, electron densities, and electric-field response properties.

INTRODUCTION

Polymer blending and inorganic modification provide complementary approaches to controlling interfacial properties in porous membranes. In systems comprising poly(lactic acid) (PLA), polycaprolactone (PCL), poly(ethylene glycol) (PEG), and nanozeolite, relevant molecular interactions involve polyester functional groups, ether-containing segments, and charged or hydrated mineral sites. Understanding the responses of these components to an applied electric field requires a molecular-level description that preserves their chemical identities while remaining computationally tractable. The central modeling challenge is therefore to establish a relationship among interfacial contact geometry, applied electric-field strength, and interaction energy, while deriving atomic forces and electric-field response properties from a consistent energy expression. Such a framework can facilitate the interpretation of membrane fabrication processes, provided that its relationship to macroscopic membrane formation is explicitly established.

Recent studies on porous polyester materials have demonstrated the importance of polymer composition and phase-separation pathways in determining membrane morphology. Damonte et al., (2022) fabricated porous PLA/PCL films incorporating graphite nanoplatelets through phase inversion, producing asymmetric porous structures with the added components dispersed throughout the polymer matrix. (Manholi & Athiyanathil, 2022) investigated PCL membranes and demonstrated that solvent selection influenced precipitation kinetics and the resulting membrane morphology. These findings highlight the importance of examining molecular interfacial interactions alongside the physicochemical environment in which the polymer-rich phase develops. They also emphasize that molecular interaction energies and final membrane pore structures represent distinct levels of description within the membrane formation process.

PEG introduces ether functional groups and conformational flexibility into polyester-based systems, although its interfacial behavior depends on molecular architecture. Wang et al., (2022) investigated PCL-block-PEG (PCL-b-PEG) oligomers and their ion-functionalized derivatives as interfacial modifiers in PLA/PCL blends, demonstrating associations between their incorporation and changes in interfacial organization and crystallization behavior. However, ion-functionalized block oligomers differ chemically from unmodified PEG, and their quantitative behavior cannot be directly extrapolated to the present formulation. Consequently, molecular modeling requires explicit specification of polymer chain lengths, terminal functional groups, and accessible molecular conformations. Interactions involving polyester carbonyl groups and PEG ether groups can then be evaluated and compared using well-defined, reproducible molecular configurations.

Nanozeolite introduces an additional class of interfaces whose physicochemical properties depend on framework composition, charge-compensating cations, and hydration conditions. Previous investigations of PEG and NaY zeolite as modifiers of membranes derived from waste poly(ethylene terephthalate) have provided related evidence supporting the combined consideration of hydrophilic additives and zeolitic materials. However, electronic-structure calculations require more precise structural definitions than a generic zeolite designation because the selected adsorption site, framework composition, and local electrostatic environment influence the reference electronic system. Stanciakova et al., (2021)

evaluated density functional approximations for water–zeolite interactions and demonstrated that adsorption-energy predictions were sensitive to the computational methodology. Accordingly, hydration conditions and the selection of exchange–correlation functionals should be treated as controlled variables during atomistic model calibration.

Electric-field-assisted nonsolvent-induced phase separation (EFA-NIPS) incorporates an externally applied electric field into the membrane casting and coagulation process. Kurniawan & Chu, (2024) investigated electric-field pretreatment during poly(vinylidene fluoride) (PVDF) membrane fabrication and examined its effects on membrane morphology and performance. At the continuum scale, (Cervellere et al., 2021) employed a phase-field model of the polyethersulfone/N-methyl-2-pyrrolidone/water system to simulate nonsolvent-induced phase separation (NIPS), comparing the numerical predictions with experimental observations. Collectively, these studies support a multiscale interpretation in which electronic responses describe localized molecular interactions, whereas phase separation describes the spatial and temporal evolution of a multicomponent mixture. The fabrication voltage considered in the present study was 10 kV. However, determining the corresponding nominal electric-field strength requires specification of the electrode separation, while the local electric-field distribution additionally depends on the electrical properties of the casting medium and electrode geometry.

Density functional theory (DFT) provides a computational framework for determining optimized interfacial geometries, electron-density distributions, and interaction-induced electric-field response properties. Li, (2021) combined dispersion-corrected DFT calculations with reactive molecular dynamics simulations to investigate PLA–attapulgite interactions, demonstrating the applicability of electronic-structure methods to polymer–mineral interfaces. For multicomponent membrane systems, reliable comparisons of interaction energies require consistent treatment of fragment geometries, electronic charges, applied electric fields, and basis-set conventions. The evaluation of basis-set superposition error and counterpoise correction by (Gray & Herbert, 2024) provides relevant methodological guidance for such calculations. Electric dipole moments, polarizabilities, and geometry-relaxation contributions can subsequently be derived from a common energy representation through appropriate differentiation, ensuring consistency among the calculated response properties.

The Lagrangian formulation provides the variational foundation required to establish a consistent electronic-structure and interfacial energy model. The hierarchy of physical energy scales discussed by Isidori et al., (2024) provides a broader theoretical context for distinguishing the low-energy electromagnetic interactions relevant to molecular systems from the full Standard Model description. At the molecular scale, a nonrelativistic electronic Hamiltonian, combined with constrained energy minimization, provides the basis for deriving electron-density and orbital stationarity equations. (Colò & Hagino, 2023) discussed the theoretical relationship between orbital-based and orbital-free density-functional approaches. Within the present framework, Lagrange multipliers enforce electron-number conservation and orbital orthonormality constraints, while the Hessian of the energy with respect to structural coordinates provides information about local structural stability. This formulation establishes a consistent theoretical foundation linking electronic-structure calculations with subsequent approximations of polymer–nanozeolite interfacial energetics.

Recent methodological advances have also demonstrated that validating a compact analytical energy expression differs fundamentally from establishing the transferability of a density functional. Kirkpatrick et al., (2021) incorporated fractional-electron constraints into a machine-learned density functional, while (Zhang et al., 2024) developed a machine-learned kinetic-energy representation for molecular orbital-free DFT. In the context of analytical interaction potentials, (Hernandez & Mueller, 2023) investigated the generalizability of functional forms identified through symbolic regression. These studies underscore the importance of evaluating physical constraints, numerical stability, and predictive performance using configurations beyond those employed for parameter estimation. For a density-functional correction, the proposed energy expression must additionally admit a well-defined functional derivative with respect to the electron density, enabling its incorporation into a stable, self-consistent electronic-structure calculation.

The present study integrates these theoretical and computational considerations into a variational framework for describing PLA/PCL/PEG–nanozeolite interfaces under an externally applied electric field. Specifically, it aims to derive a consistent interfacial energy expression, distinguish fixed-geometry (clamped-coordinate) electric-field responses from geometry-relaxation contributions, and quantify the effects of numerical differentiation errors and higher-order truncation on the estimated response coefficients. The proposed atomistic reference workflow provides a basis for subsequent parameter calibration and evaluation of model transferability across different interfacial contact geometries and hydration conditions. The principal contribution of this study is the development of a reproducible and differentiable interfacial energy model with an explicitly defined domain of applicability and a systematic pathway toward extension into a self-consistent density-functional framework.

METHOD

Molecular setup and variational foundation

The atomistic reference protocol was designed to investigate optimized PLA/PCL/PEG–nanozeolite interfaces. Avogadro was designated for molecular structure preparation, while ORCA was selected for geometry optimization at the PBE0-D3(BJ)/def2-SVP level of theory, followed by single-point energy calculations using the def2-TZVPD basis set (Neese, 2022). The analytical demonstrations and response coefficient fitting were performed using Python with NumPy and SciPy. The reference models were specified in terms of oligomer chain length, zeolite framework composition, charge-balancing cations, hydration state, total charge, and spin multiplicity, with appropriate constraints applied to the zeolite framework boundaries. The proposed atomistic calculations were intended for subsequent calibration and validation of the analytical interfacial energy model.

$$N_e = \sum_A Z_A - Q. \qquad (1)$$

$$\mathbf{R}^*(\mathbf{F}) = \underset{\mathbf{R}\in\mathcal{C}\cap\mathcal{U}}{\operatorname{argmin}} E_{\mathrm{BO}}(\mathbf{R},\mathbf{F}). \qquad (2)$$

$$F_{\mathrm{nom}} = \frac{V}{d} = \frac{10^4}{d}\ \mathrm{V\,m^{-1}}. \qquad (3)$$

$$\nabla\cdot[\varepsilon_0\varepsilon_r(\mathbf{r})\nabla\phi(\mathbf{r})] = 0. \qquad (4)$$

$$\mathbf{F}(\mathbf{r}) = -\nabla\phi(\mathbf{r}). \qquad (5)$$

$$F_{\mathrm{au}} = \frac{F_{\mathrm{SI}}}{5.1422067\times10^{11}\ \mathrm{V\,m^{-1}}}. \qquad (6)$$

Nuclear charges determine N_e; Q is net charge, C the constraints and U a local conformational basin. V = 10 kV, d is electrode spacing, φ electrostatic potential and ε_r relative permittivity. The field mapping assumes a charge-free dielectric continuum; conductive media require charge/current conservation. Complexes and fragments share the same external field and origin.

$$\mathcal{L}_{\mathrm{em}} = -\frac{1}{4}F_{\mu\nu}F^{\mu\nu} + \bar{\psi}(i\gamma^{\mu}D_{\mu} - m_e)\psi + \mathcal{L}_{\mathrm{nuc}}. \quad (7)$$

$$F_{\mu\nu} = \partial_{\mu}A_{\nu} - \partial_{\nu}A_{\mu}, \qquad D_{\mu} = \partial_{\mu} + iqA_{\mu}. \quad (8)$$

$$S = \int \mathcal{L}_{\mathrm{em}}\, d^4x, \qquad \delta S = 0. \quad (9)$$

$$\frac{\partial \mathcal{L}_{\mathrm{em}}}{\partial \bar{\psi}} - \partial_{\mu}\left[\frac{\partial \mathcal{L}_{\mathrm{em}}}{\partial(\partial_{\mu}\bar{\psi})}\right] = 0. \quad (10)$$

$$(i\gamma^{\mu}D_{\mu} - m_e)\psi = 0. \quad (11)$$

The electromagnetic sector uses the electron field ψ, its adjoint, four-potential A and charge q = −e. The nonrelativistic molecular approximation retains electrons and effective nuclei, consistent with the scale separation discussed by Isidori et al. (2024) Molecular equations below use atomic units.

$$\widehat{H}_0 = \sum_{i=1}^{N_e}\left[-\frac{1}{2}\nabla_i^2 + v_{\mathrm{nuc}}(\mathbf{r}_i)\right] + \sum_{i<j}\frac{1}{r_{ij}} + E_{nn}. \quad (12)$$

$$v_{\mathrm{nuc}}(\mathbf{r}) = -\sum_A \frac{Z_A}{|\mathbf{r}-\mathbf{R}_A|}, \qquad E_{nn} = \sum_{A<B}\frac{Z_A Z_B}{R_{AB}}. \quad (13)$$

$$\widehat{\boldsymbol{\mu}} = \sum_A Z_A\,\mathbf{R}_A - \sum_{i=1}^{N_e}\mathbf{r}_i. \quad (14)$$

$$\widehat{H}_{\mathbf{F}} = \widehat{H}_0 - \mathbf{F}\cdot\widehat{\boldsymbol{\mu}}. \quad (15)$$

$$E_0(\mathbf{R},\mathbf{0}) = \min_{\Psi\in\mathcal{H}_{N_e},\langle\Psi|\Psi\rangle=1}\langle\Psi|\widehat{H}_0|\Psi\rangle. \quad (16)$$

Density functional formulation and numerical solution

The antisymmetric wavefunction Ψ and orbital density n define the variational problem. Orbitals φ_i have occupations f_i; spin-resolved densities apply to open-shell cases. The exact density functional and its constrained Euler equation are written first, following Colò & Hagino (2023).

$$n(\mathbf{r}) = \sum_i f_i\,|\varphi_i(\mathbf{r})|^2, \qquad \int n(\mathbf{r})\,d\mathbf{r} = N_e. \quad (17)$$

$$F_{\mathrm{HK}}[n] = \min_{\Psi\to n}\langle\Psi|\hat{T}_e + \hat{V}_{ee}|\Psi\rangle. \quad (18)$$

$$E[n;\mathbf{R},\mathbf{F}] = F_{\mathrm{HK}}[n] + \int v_{\mathrm{nuc}} n\,d\mathbf{r} + E_{nn} - \mathbf{F}\cdot\boldsymbol{\mu}[n]. \quad (19)$$

$$F_{\mathrm{HK}}[n] = T_s[n] + E_H[n] + E_{xc}[n]. \quad (20)$$

$$T_s = -\frac{1}{2}\sum_i f_i \int \varphi_i^*(\mathbf{r})\nabla^2\varphi_i(\mathbf{r})\,d\mathbf{r}. \quad (21)$$

$$E_H[n] = \frac{1}{2}\iint \frac{n(\mathbf{r})n(\mathbf{r}')}{|\mathbf{r}-\mathbf{r}'|}\,d\mathbf{r}\,d\mathbf{r}'. \quad (22)$$

$$\boldsymbol{\mu}[n] = \sum_A Z_A\,\mathbf{R}_A - \int \mathbf{r}\,n(\mathbf{r})\,d\mathbf{r}. \quad (23)$$

$$\mathcal{L}_n = E[n] - \eta\left[\int n\,d\mathbf{r} - N_e\right], \qquad \frac{\delta\mathcal{L}_n}{\delta n} = 0. \quad (24)$$

$$\frac{\delta T_s}{\delta n(\mathbf{r})} + v_{\mathrm{nuc}} + v_H + v_{xc} + \mathbf{F}\cdot\mathbf{r} = \eta. \quad (25)$$

The energy comprises non-interacting kinetic, Hartree and exchange–correlation terms; η is the electron-number multiplier and μ the total dipole. The orbital-dependent hybrid

enforces orbital orthonormality through matrix Λ. The GKS matrix, overlap matrix and orbital coefficients are H, S and C; their density dependence requires SCF iteration.

$$E_{\mathrm{calc}} = T_s + E_H + E_{xc}^{\mathrm{hyb}} + \int v_{\mathrm{nuc}} n \, d\mathbf{r} + E_{nn} + E_{\mathrm{D3(BJ)}} - \mathbf{F}\cdot\boldsymbol{\mu}. \quad (26)$$

$$E_{xc}^{\mathrm{PBE0}} = \frac{1}{4}E_x^{\mathrm{HF}} + \frac{3}{4}E_x^{\mathrm{PBE}} + E_c^{\mathrm{PBE}}. \quad (27)$$

$$\mathcal{L}_{\mathrm{orb}} = E_{\mathrm{calc}} - \sum_{ij} \Lambda_{ij}\,[\langle\varphi_i|\varphi_j\rangle - \delta_{ij}]. \quad (28)$$

$$[-\tfrac{1}{2}\nabla^2 + v_{\mathrm{nuc}} + v_H + \hat{v}_{xc}^{\mathrm{hyb}} + \mathbf{F}\cdot\mathbf{r}]\varphi_i = \epsilon_i\varphi_i. \quad (29)$$

$$\mathbf{H}_{\mathrm{GKS}}\mathbf{C} = \mathbf{S}\mathbf{C}\boldsymbol{\epsilon}, \qquad \mathbf{C}^{\dagger}\mathbf{S}\mathbf{C} = \mathbf{I}. \quad (30)$$

$$\mathbf{g}_{\mathrm{free}} = \nabla_{\mathbf{R}_{\mathrm{free}}} E_{\mathrm{BO}}, \qquad \|\,\mathbf{g}_{\mathrm{free}}\,\|_{\infty} < 3\times10^{-5}\ \mathrm{hartree\,bohr^{-1}}. \quad (31)$$

$$(H_q)_{ab} = \frac{\partial^2 E_{\mathrm{BO}}}{\partial q_a\,\partial q_b}, \qquad \lambda_{\mathrm{vib}}(\mathbf{H}_q) > 0. \quad (32)$$

DEFGRID3 and an SCF energy threshold of 10^{-10} hartree will be used, with tighter checks for response calculations. The gradient and Hessian tests apply to permitted internal coordinates after removing rigid modes. Basis/cluster sensitivity targets are 1 kJ mol^{-1} in interaction energy and 5% in response. Functional sensitivity is assessed separately; see Stanciakova et al. (2021).

Interfacial energies and electric field response

B denotes the full complex basis, including ghost functions; b_k is a fragment basis. Charges, geometry and field are matched across subsets, and ghost centres are excluded as physical dispersion sites. Interaction, deformation and binding energies follow the stated counterpoise convention; see Gray et al. (2022).

$$E_{\mathrm{int}}^{\mathrm{CP}}(\mathbf{F}) = E_C^B(\mathbf{F}) - \sum_{k=1}^{K} E_k^B\,(\mathbf{F}). \quad (33)$$

$$E_{\mathrm{def}}(\mathbf{F}) = \sum_k [E_k^{b_k}(\mathbf{R}_k^C, \mathbf{F}) - E_k^{b_k}(\mathbf{R}_k^*, \mathbf{F})]. \quad (34)$$

$$E_{\mathrm{bind}}^{\mathrm{CP}} = E_{\mathrm{int}}^{\mathrm{CP}} + E_{\mathrm{def}}. \quad (35)$$

$$\Delta n(\mathbf{r}) = n_C(\mathbf{r}) - \sum_k n_k\,(\mathbf{r}), \qquad \int \Delta n(\mathbf{r})\,d\mathbf{r} = 0. \quad (36)$$

$$\Delta E_{ij}^B = E_{ij}^B - E_i^B - E_j^B. \quad (37)$$

$$E_{\mathrm{nonadd}} = E_{\mathrm{int}}^{\mathrm{CP}} - \sum_{i<j} \Delta\, E_{ij}^B. \quad (38)$$

Δn is the complex-minus-fragment density at conserved electron number; nonadditivity measures contributions beyond matched pairs. For fixed geometry, dipoles and clamped-nuclei polarisabilities follow energy derivatives. In Eq. (43), E_{st} = E(sh e_a + th e_β), with s,t = ±1. Numerical field steps are probes, distinct from the fabrication field.

$$E(\mathbf{R},\mathbf{F}) = E(\mathbf{R},\mathbf{0}) - \boldsymbol{\mu}_0\cdot\mathbf{F} - \tfrac{1}{2}\mathbf{F}^T\boldsymbol{\alpha}^{\mathrm{el}}\mathbf{F} + O(|\mathbf{F}|^3). \quad (39)$$

$$\mu_a = -\frac{\partial E}{\partial F_a}\Big|_{\mathbf{R}}, \qquad \alpha_{ab}^{\mathrm{el}} = -\frac{\partial^2 E}{\partial F_a\,\partial F_b}\Big|_{\mathbf{R}}. \quad (40)$$

$$\mu_a \approx -\frac{E(h\mathbf{e}_a) - E(-h\mathbf{e}_a)}{2h}. \quad (41)$$

$$\alpha_{aa}^{\mathrm{el}} \approx -\frac{E(h\mathbf{e}_a) - 2E(\mathbf{0}) + E(-h\mathbf{e}_a)}{h^2}. \quad (42)$$

$$\alpha_{ab}^{\mathrm{el}} \approx -\frac{E_{++} - E_{+-} - E_{-+} + E_{--}}{4h^2}. \quad (43)$$

$$E_{\mathrm{rel}}(\mathbf{F}) = E_{\mathrm{BO}}(\mathbf{R}^*(\mathbf{F}),\mathbf{F}), \qquad \alpha_{ab}^{\mathrm{rel}} = -\frac{d^2 E_{\mathrm{rel}}}{dF_a\,dF_b}. \quad (44)$$

$$\boldsymbol{\alpha}^{\mathrm{rel}} = \boldsymbol{\alpha}^{\mathrm{el}} + \mathbf{K}^T\mathbf{H}_q^{-1}\mathbf{K}, \qquad K_{ab} = \frac{\partial \mu_b}{\partial q_a}. \quad (45)$$

Steps h = 10^{-4}, 5×10^{-5} and 2.5×10^{-5} a.u. will be checked against SCF precision and tensor symmetry. Hq and K describe curvature and dipole gradients in the same free-coordinate subspace; Eq. (45) requires a stable harmonic minimum. Electronic response, field-relaxed response and relaxation after field removal will be assessed separately, following the field-response context of Daub & Kurtén (2024).

Analytical equation and independent validation

Descriptors x encode contacts, orientations, chemical identities and hydration. The functions g, m and A represent zero-field interaction energy and interaction-induced dipole/polarisability. Responses derive from one energy expression; scalar rotation invariance, tensor covariance, dissociation and dimensional consistency constrain the search. Compact forms follow Hernandez & Mueller (2023).

$$E_\theta^{\mathrm{int}}(\mathbf{x},\mathbf{F}) = g_\theta(\mathbf{x}) - \mathbf{m}_\theta(\mathbf{x})\cdot\mathbf{F} - \frac{1}{2}\mathbf{F}^T\mathbf{A}_\theta(\mathbf{x})\mathbf{F}. \quad (46)$$

$$g_\theta(\mathbf{x}) = \sum_{\ell=1}^{L} c_\ell\ \phi_\ell(\mathbf{x}). \quad (47)$$

$$\Delta\boldsymbol{\mu}_\theta = -\nabla_{\mathbf{F}} E_\theta^{\mathrm{int}}, \qquad \Delta\boldsymbol{\alpha}_\theta = -\nabla_{\mathbf{F}}\nabla_{\mathbf{F}} E_\theta^{\mathrm{int}}. \quad (48)$$

$$J(\theta) = \sum_{p\in\{E,\mu,\alpha\}} \frac{w_p}{M_p s_p^2} \sum_{j=1}^{M_p} \| \mathbf{y}_{jp} - \hat{\mathbf{y}}_{jp}(\theta) \|^2 + \lambda C(\theta). \quad (49)$$

$$E_\theta^{\mathrm{int}}(\mathbf{x}(\mathbf{QR}),\mathbf{QF}) = E_\theta^{\mathrm{int}}(\mathbf{x}(\mathbf{R}),\mathbf{F}). \quad (50)$$

$$\lim_{D_{\mathrm{sep}}\to\infty} E_\theta^{\mathrm{int}}(\mathbf{x},\mathbf{F}) = 0. \quad (51)$$

The objective uses training-set scales s_p, property weights w_p, sample counts M_p and complexity C. A is symmetric but, as an interaction difference, need not be positive definite. A self-consistent density-functional extension additionally requires an explicit correction and its variational potential:

$$\Delta E_\theta[n] = \int f_\theta(n(\mathbf{r}), \nabla n(\mathbf{r}))\, d\mathbf{r}. \quad (52)$$

$$\Delta v_\theta(\mathbf{r}) = \frac{\partial f_\theta}{\partial n} - \nabla\cdot\left(\frac{\partial f_\theta}{\partial(\nabla n)}\right). \quad (53)$$

$$[\hat{h}_{\mathrm{GKS}}^{\mathrm{base}} + \Delta v_\theta(\mathbf{r})]\varphi_i = \epsilon_i\varphi_i. \quad (54)$$

The derivative assumes vanishing density variations at the boundary. Eq. (54) specifies an implementation requirement rather than a fitted result. Physical constraints and density-level validation are essential; see Kirkpatrick et al. (2021).

$$\mathrm{MAE} = \frac{1}{M}\sum_{j=1}^{M} |y_j - \hat{y}_j|. \quad (55)$$

$$\mathrm{RMSE} = \left[\frac{1}{M}\sum_{j=1}^{M}(y_j - \hat{y}_j)^2\right]^{1/2}. \quad (56)$$

$$R^2 = 1 - \frac{\sum_j (y_j - \hat{y}_j)^2}{\sum_j (y_j - \bar{y})^2}. \quad (57)$$

Parent interfaces, conformers and hydration classes will define grouped training/validation/test partitions, initially 70/15/15. Related field points remain grouped. Errors in energy, dipoles and tensors will be reported separately, with group resampling where feasible. Coordinates, partitions, fitting settings, coefficients and scripts will be archived. PySCF is an option for implementing a density correction; it is not required for the ORCA reference workflow.

Derivation of the stationary DFT equations

The first variation of Eq. (24) is taken at fixed nuclei and applied field. The Hartree derivative follows directly from Eq. (22); the constant nuclear energy has no density variation.

$$\delta\mathcal{L}_n = \int [\tfrac{\delta F_{\mathrm{HK}}}{\delta n} + v_{\mathrm{nuc}} + \mathbf{F}\cdot\mathbf{r} - \eta]\delta n\, d\mathbf{r}. \quad (58)$$

$$\tfrac{\delta E_{\mathrm{H}}}{\delta n(\mathbf{r})} = v_{\mathrm{H}}(\mathbf{r}) = \int \tfrac{n(\mathbf{r}')}{|\mathbf{r}-\mathbf{r}'|}\, d\mathbf{r}'. \quad (59)$$

$$\delta\mathcal{L}_n = 0 \;\Rightarrow\; \tfrac{\delta T_s}{\delta n} + v_{\mathrm{nuc}} + v_{\mathrm{H}} + v_{\mathrm{xc}} + \mathbf{F}\cdot\mathbf{r} = \eta. \quad (60)$$

For a closed-shell occupied subspace with common occupation f, absorb f into the orbital multipliers. A unitary transformation diagonalises the multiplier matrix, after which basis projection gives the generalised eigenvalue problem.

$$\tfrac{1}{f}\tfrac{\delta\mathcal{L}_{\mathrm{orb}}}{\delta\varphi_i^*} = \hat{h}_{\mathrm{GKS}}\varphi_i - \textstyle\sum_j \lambda_{ij}\,\varphi_j = 0, \qquad \lambda_{ij} = \Lambda_{ij}/f. (61)$$

$$\varphi_i = \textstyle\sum_\nu C_{\nu i}\,\chi_\nu, \qquad H_{\mu\nu} = \langle\chi_\mu|\hat{h}_{\mathrm{GKS}}|\chi_\nu\rangle, \qquad S_{\mu\nu} = \langle\chi_\mu|\chi_\nu\rangle. \quad (62)$$

$$\langle\chi_\mu|\hat{h}_{\mathrm{GKS}}|\varphi_i\rangle = \epsilon_i\langle\chi_\mu|\varphi_i\rangle \;\Rightarrow\; \textstyle\sum_\nu H_{\mu\nu}\,C_{\nu i} = \epsilon_i \sum_\nu S_{\mu\nu}\,C_{\nu i}. \quad (63)$$

$$P_{\mu\nu} = \textstyle\sum_i f_i\, C_{\mu i}C_{\nu i}^*, \qquad n(\mathbf{r}) = \textstyle\sum_{\mu\nu} P_{\mu\nu}\,\chi_\mu(\mathbf{r})\chi_\nu^*(\mathbf{r}). (64)$$

$$H[P^{(k)}]C^{(k+1)} = SC^{(k+1)}\epsilon^{(k+1)}, \qquad |E^{(k+1)} - E^{(k)}| < 10^{-10}E_{\mathrm{h}}. \quad (65)$$

Equations (64)–(65) close the density–Hamiltonian iteration; energy convergence is checked together with orbital and density residuals. For the density correction in Eq. (52), integration by parts gives its variational potential explicitly.

$$\delta\Delta E_\theta = \textstyle\int_\Omega [\tfrac{\partial f_\theta}{\partial n}\delta n + \tfrac{\partial f_\theta}{\partial(\nabla n)}\cdot\nabla\delta n]\, d\mathbf{r}. (66)$$

$$\textstyle\int_\Omega \tfrac{\partial f_\theta}{\partial(\nabla n)}\cdot\nabla\delta n\, d\mathbf{r} = \int_{\partial\Omega}\delta\, n\,\tfrac{\partial f_\theta}{\partial(\nabla n)}\cdot\hat{\mathbf{v}}\, dS$$

$$- \textstyle\int_\Omega \nabla\cdot[\tfrac{\partial f_\theta}{\partial(\nabla n)}]\delta n\, d\mathbf{r},$$

$$\Delta v_\theta = \tfrac{\partial f_\theta}{\partial n} - \nabla\cdot[\tfrac{\partial f_\theta}{\partial(\nabla n)}] \quad (\delta n|_{\partial\Omega} = 0). \quad (67)$$

The boundary term vanishes for δn = 0 on ∂Ω. This derivation supplies the potential required by Eq. (54); fitting an interfacial energy alone does not determine the density-dependent integrand fθ.

RESULTS AND DISCUSSION

C1–C3 represent PLA–Z, PCL–Z and PEG–Z contacts; C4 is the polymer blend and C5 the blend–Z contact, where Z denotes zeolite. The coordinate q is dimensionless.

Table 1. Assigned parameters for the five interface models.

Interface	D / kJ mol⁻¹	a	μ₀ / D	α₀ / a.u.	ζ / 10⁻⁵ kJ mol⁻¹
C1 PLA–Z	32.40	2.15	1.80	90	1.50
C2 PCL–Z	24.70	1.75	1.35	105	1.20
C3 PEG–Z	41.80	2.35	2.45	120	2.00
C4 PLA/PCL/PEG	53.60	1.90	2.10	205	3.00
C5 PLA/PCL/PEG–Z	91.30	2.55	4.25	310	5.00

The generating equation combines the contact well and field response:

$$E_M(q,F) = D(s^2 - 2s) - K_E(\tilde{\mu}\, tF + \tfrac{1}{2}\alpha\, t^2F^2) - \zeta\, t^3f^4. \quad (68)$$

$$s = e^{-a(q-1)}, \qquad t = e^{-b(q-1)}, \qquad f = F/F_s. \quad (69)$$

Here b = 0.75, $F_s = 10^{-4}$ a.u. and $K_e = 2625.49964$ kJ mol^{-1} per hartree. The atomic-unit dipole is the tabulated Debye value divided by 2.541746473. NumPy evaluates the functions; SciPy locates stationary contacts from the analytical gradient.

$$E_0(q) = D(s^2 - 2s), \qquad \frac{dE_0}{dq} = 2Da(s - s^2) = 2Da\,s(1 - s). \quad (70)$$

$$\frac{d^2E_0}{dq^2} = 2Da^2(2s^2 - s), \qquad k = \frac{d^2E_0}{dq^2}\Big|_{q=1} = 2Da^2 > 0. \quad (71)$$

$$\frac{dE_0}{dq} = 0 \;\Rightarrow\; s = 1 \;\Rightarrow\; q_* = 1, \qquad E_0(q_*) = -D. \quad (72)$$

$$E_{0,5}(1) = -91.30\ \text{kJ mol}^{-1}, \qquad k_5 = 2(91.30)(2.55)^2 = 1187.3565\ \text{kJ mol}^{-1}. \quad (73)$$

Well depth and contact curvature describe different features of the assigned landscape. The C5 well is 1.70 times deeper than C4, while its curvature is 3.07 times larger. Thus, the energy gained on contact formation and the resistance to a small displacement do not increase in the same proportion. C2 has the shallowest and softest well. All five curvatures are positive, establishing local minima in q. Because q is dimensionless, conversion to a stiffness per physical distance additionally requires the length scale used to define that coordinate.

A deeper combined well alone does not establish cooperative binding. Equations (37)–(38) require energies of matched subsets at the same geometry, field and basis convention; the five independently assigned well depths do not provide that decomposition. This distinction separates a ranking within the numerical demonstration from a chemical assignment of nonadditivity. For atomistic calibration, the zeolite site and hydration state must also be fixed. The water–zeolite calculations of Stanciakova et al. (2021) provide related evidence that adsorption descriptions depend on the selected electronic-structure treatment.

Energy landscape and electrical perturbation

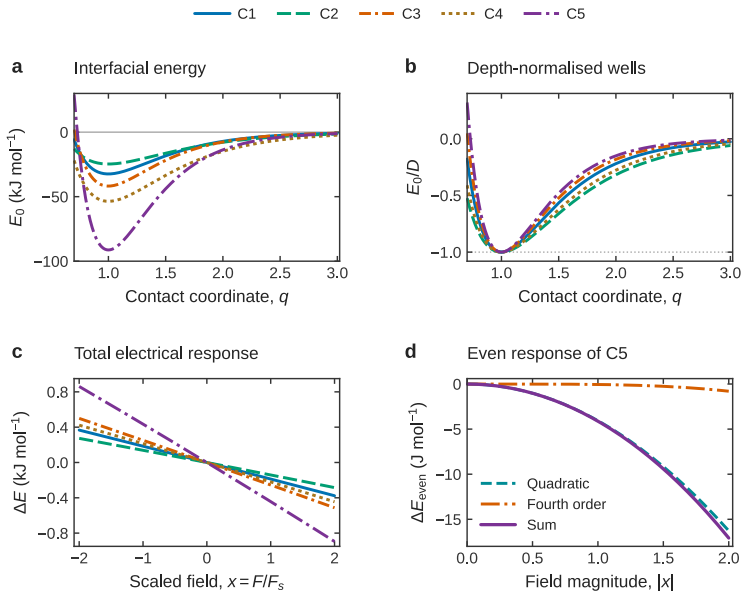


Figure 1. (a) Zero-field interaction energies. (b) Wells normalised by D. (c) Fixed-coordinate field-induced energy shifts at q = 1. (d) C5 even response separated into quadratic, fourth-order and total contributions. $F_s = 10^{-4}$ a.u. Colours and line patterns identify the cases in Table 1.

Figure 1a shows that each assigned contact approaches the same dissociation reference, zero energy, as q increases. At short separation, the repulsive exponential rises more rapidly than the attractive term; their balance fixes the minimum at q = 1. The common minimum position is imposed by the coordinate definition and does not mean that the five chemical contacts have identical physical equilibrium distances. Their distinct depths and widths remain independent parameters of the demonstration.

Normalisation in Figure 1b removes D and isolates the width parameter a. The curvature of a depth-normalised well is proportional to a^2, so a deeper contact need not have the same relative width as a shallower one. C5 combines the largest depth with the largest a and therefore shows the strongest local resistance to displacement. C4, although deeper than the three individual polymer–zeolite models, has a smaller a than C1 and C3. This explains why the rankings by depth and by curvature differ.

Energy references and field symmetry

The decay factors in Eq. (69) also provide a consistent dissociation limit for the field response: the assigned dipolar, quadratic and fourth-order contributions vanish with increasing separation. If the model is calibrated to an interaction energy, its field derivatives must represent the response associated with forming that interaction. Total-complex dipoles and polarisabilities would require field-matched fragment subtraction before use as those parameters. This follows the same reference-state logic as the interaction energies in Eqs. (33)–(38); the counterpoise assessment of Gray & Herbert (2024) supports maintaining a consistent basis convention.

The leading field response in Figure 1c is odd in F. At q = 1, taking half the difference between positive- and negative-field energy shifts isolates the dipolar term, whereas half their sum isolates the even response in Figure 1d. The latter contains both the quadratic and fourth-order contributions. This separation explains why a nearly straight total-energy curve can still contain a measurable numerical bias in a response coefficient extracted from its curvature.

For C5 at the positive probe field, the three contributions are −439.00419, −4.06952 and −0.05000 J mol^{-1}, respectively, giving the total shift of −443.12371 J mol^{-1}. The fourth-order term is only 1.23% of the quadratic term at this probe, but that proportion increases to 4.91% at twice the probe magnitude. A quadratic approximation consequently represents the dominant energy shift well while progressively misrepresenting the smaller even component. The relevant accuracy criterion depends on whether the target is total energy or a second derivative.

The probe field is 154.27 times the nominal field obtained from 10 kV over an assumed 3 cm gap. At the nominal field, the C5 quadratic contribution is about 6.01×10^{-5} of the dipolar contribution, and the total shift is only 0.00312% of D. Dipole-dominated weak-field behaviour has also been reported for the molecular clusters examined by Daub & Kurtén (2024). That study provides a field-response comparison; its cluster compositions and numerical energies are separate from the present polymer–zeolite model.

The scalar field in this demonstration is aligned with the selected model dipole. Changing orientation changes the dipolar projection, while a tensor treatment is required to compare anisotropic polarisabilities. The nominal voltage therefore specifies neither the local field nor an orientationally averaged molecular response by itself. During EFA-NIPS, dielectric contrast, electrode geometry and charge transport may alter the field experienced by a contact.

The present calculation resolves the response of a specified contact to a supplied field; connecting it to phase separation requires the additional spatial description introduced in Eqs. (3)–(6).

Derivation of field response and contact relaxation

Expand Eq. (68) near q = 1 to second order, with k = 2Da² and μ̃′₀ = −bμ̃₀. Minimising the expansion over the contact displacement gives the relaxed response.

$$E(q,F) \simeq -D + \frac{k}{2}\delta q^2 - K_E\tilde{\mu}_0 F - K_E\tilde{\mu}'_0\delta q F - \frac{K_E}{2}\alpha_0 F^2, \qquad \delta q = q - 1. \quad (74)$$

$$\frac{\partial E}{\partial \delta q} = k\delta q - K_E\tilde{\mu}'_0 F = 0 \;\Rightarrow\; \delta q_* = -\frac{K_E b\tilde{\mu}_0}{k}F. \qquad (75)$$

$$E_{\mathrm{rel}}(F) = -D - K_E\tilde{\mu}_0 F - \frac{K_E}{2}[\alpha_0 + \frac{K_E(\tilde{\mu}'_0)^2}{k}]F^2 + O(F^3). \quad (76)$$

$$\alpha_{\mathrm{rel}} = \alpha_0 + \frac{K_E b^2\tilde{\mu}_0^2}{2Da^2}, \qquad \alpha_{\mathrm{rel},5} = 310.00000 + 3.47750 = 313.47750\ \mathrm{a.u.} \quad (77)$$

$$F_{\mathrm{nom}} = \frac{10^4}{0.03} = 3.33333 \times 10^5\ \mathrm{V\,m^{-1}} = 6.48230 \times 10^{-7}\ \mathrm{a.u.} \qquad (78)$$

$$\Delta E_5(F_{\mathrm{nom}}) \simeq -2.8457574 - 0.0001710 - 8.83 \times 10^{-11} \simeq -2.8459284\ \mathrm{J\,mol^{-1}}. \quad (79)$$

Contact compliance and numerical differentiation

Table 2. Field shifts at q = 1 and geometry-relaxed responses. F nominal is 6.4823 × 10⁻⁷ a.u. for 10 kV over an assumed 3 cm gap; the probe is 10⁻⁴ a.u. Displacements are stationary points of the full analytical potential.

Case	ΔE nominal / J mol⁻¹	ΔE probe / kJ mol⁻¹	α relaxed / a.u.	10⁶ × Δq nominal
C1	-1.2053	-0.187128	92.473	-3.018
C2	-0.9040	-0.140839	107.754	-4.482
C3	-1.6406	-0.254668	122.972	-2.665
C4	-1.4063	-0.219641	207.605	-2.726
C5	-2.8459	-0.443124	313.477	-1.798

Figure 2 separates three comparisons that would be obscured by a ranking based on well depth alone. Panels a and b describe the energetic preference for contact and its local stiffness. Panel c additionally depends on the dipole gradient, and panel d reports the relative contribution of contact motion to the response. C2 has a curvature of 151.29 kJ mol⁻¹ per unit q² and a nominal displacement magnitude of 4.482 × 10⁻⁶. The stiffer C5 contact shifts by only 1.798 × 10⁻⁶ despite its larger dipole.

The negative displacement at positive field follows from the assumed decay of the dipolar contribution with separation. Moving to smaller q increases its magnitude and lowers the aligned-field energy until the restoring contact force balances the electrical force. Field reversal changes the leading displacement sign. The symbols in Figure 2c come from stationary points of the full potential and lie close to Eq. (75) at nominal-field ratios between −2 and 2. Their agreement establishes that the local linear expansion is adequate on this particular field scale. At q = 1, the fourth-order field term gives an exact central-difference bias:

$$\alpha_{\mathrm{FD}}(h) = -\frac{E(h)-2E(0)+E(-h)}{K_E h^2} = \alpha_0 + \frac{2\zeta}{K_E F_S^4} h^2. \qquad (80)$$

$$\alpha_{\mathrm{FD}}(h/2) - \alpha_0 = \frac{\alpha_{\mathrm{FD}}(h)-\alpha_0}{4}. \quad (81)$$

Table 3. Central-difference checks for C5 against the analytical derivative.

Step h / a.u.	Dipole / D	Polarisability / a.u.	Bias in α / %
1.00e-04	4.25000	313.808799	1.22864
5.00e-05	4.25000	310.952200	0.30716
2.50e-05	4.25000	310.238050	0.07679

Table 3 and Figure 3a test numerical differentiation against an analytical derivative rather than against another fitted value. For C5, the polarisability estimates decrease from 313.808799 to 310.952200 and 310.238050 a.u. as h is halved twice. The corresponding excess above 310 a.u. decreases by a factor of four at each step. Equation (80) predicts this trend exactly because the fourth-order energy contribution survives the second central difference as a term proportional to h^2.

The dipole remains 4.25 D at all three steps because the even field powers cancel in the first central difference. This exact cancellation depends on symmetric sampling and on the absence of additional odd terms at fixed q in the generating potential. It does not imply that first derivatives from atomistic calculations are automatically independent of field step. Electronic convergence, changes of structural basin and any higher odd-order response would introduce additional sources of variation.

Reducing h indefinitely would not be an appropriate numerical prescription for DFT output. The second-difference numerator scales with h^2, so a fixed error in the underlying energies is amplified as the field step becomes smaller. An atomistic calculation should therefore identify a stable interval of step sizes while tightening SCF and integration settings. The present analytical checks isolate truncation error and establish the expected trend before those electronic-structure errors are introduced.

Interfacial stiffness and structural response

The contact-relaxation term in Eq. (77) is non-negative because the dipole gradient is squared and the curvature is positive. Its absolute contribution is 3.4775 a.u. for C5, compared with 2.4727 a.u. for C1. The fractional increases have the opposite order, 1.12% and 2.75%, because C5 starts from the much larger clamped-coordinate value. Thus, the largest absolute polarisability need not identify the contact with the largest relative structural susceptibility. Both the denominator and the normalisation must be considered.

The scalar q captures one selected contact motion. In an atomistic model, the corresponding correction involves the dipole-gradient matrix and the inverse Hessian over the permitted internal-coordinate subspace, as specified in Eq. (45). Constrained zeolite atoms, end-group motion and accessible polymer conformations change that subspace. The comparison among contact classes should therefore retain consistent boundary constraints and optimisation criteria. Positive curvature establishes local stability within the selected basin; sampling other conformers remains a separate part of the reference workflow.

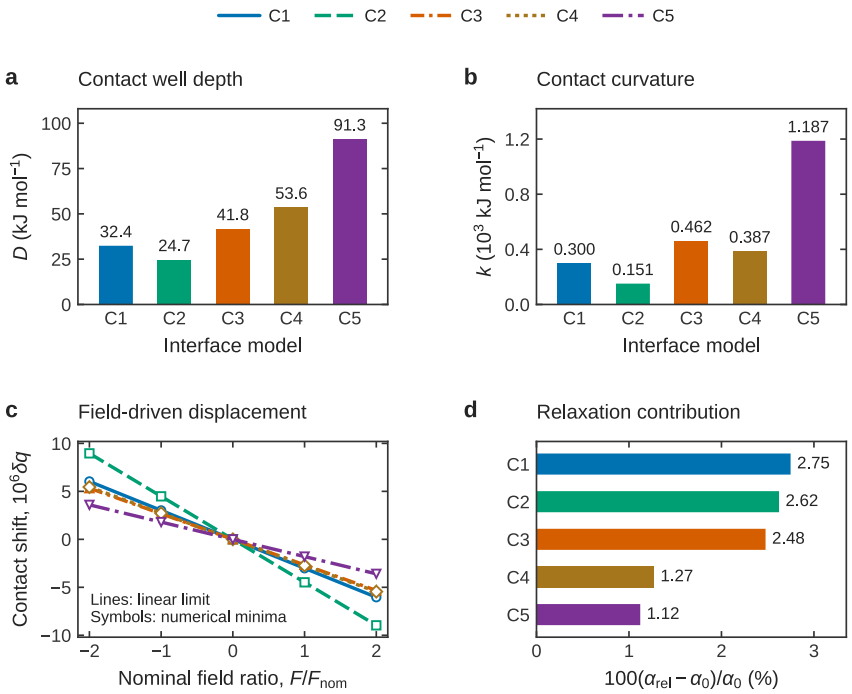


Figure 2. (a) Contact well depths. (b) Curvatures, shown in 10^3 kJ mol^{-1} per unit q^2. (c) Contact displacements: lines show the linear limit and symbols show numerical minima. (d) Fractional relaxation contribution to polarisability. F nominal corresponds to 10 kV over an assumed 3 cm gap.

Derivation and assessment of the fitted equation

At q = 1, subtract the zero-field energy and scale the field by F_s. Fit the quadratic form at x = 0, ±0.25, ±0.50 and ±1.00. Symmetric sampling decouples the odd and even coefficients.

$$x = F/F_s, \qquad y(x) = E(1,F) - E(1,0) = c_1 x + c_2 x^2 - \zeta x^4. \qquad (82)$$

$$c_1 = -K_E \tilde{\mu}_0 F_s, \qquad c_2 = -\frac{1}{2} K_E \alpha_0 F_s^2. \qquad (83)$$

$$X_j = (x_j, x_j^2), \qquad \hat{\boldsymbol{\beta}} = (X^{\mathrm{T}}X)^{-1}X^{\mathrm{T}}\mathbf{y}, \qquad \hat{y}(x) = \hat{\beta}_1 x + \hat{\beta}_2 x^2. \qquad (84)$$

$$\sum_j x_j^3 = \sum_j x_j^5 = 0 \;\Rightarrow\; \hat{\beta}_1 = c_1, \quad \hat{\beta}_2 = c_2 - \zeta\rho, \quad \rho = \frac{\sum_j x_j^6}{\sum_j x_j^4}. \qquad (85)$$

$$\hat{\tilde{\mu}}_0 = -\frac{\hat{\beta}_1}{K_E F_s} = \tilde{\mu}_0, \qquad \hat{\alpha}_0 = -\frac{2\hat{\beta}_2}{K_E F_s^2} = \alpha_0 + \frac{2\zeta\rho}{K_E F_s^2}. \qquad (86)$$

$$\rho = 0.9526098901, \qquad \hat{\alpha}_{0,5} = 310.000000 + 3.628299 = 313.628299 \text{ a.u.} \qquad (87)$$

$$r(x) = \hat{y}(x) - y(x) = \zeta(x^4 - \rho x^2), \qquad r(-x) = r(x). \qquad (88)$$

Table 4. Quadratic fits checked at x = ±0.75, ±1.50 and ±2.00.

Case	Fitted α / a.u.	MAE / J mol⁻¹	RMSE / J mol⁻¹	Max error / J mol⁻¹	R²
C1	91.088	0.07664	0.10857	0.18284	0.99999985
C2	105.871	0.06131	0.08685	0.14627	0.99999983
C3	121.451	0.10219	0.14475	0.24379	0.99999986
C4	207.177	0.15328	0.21713	0.36569	0.99999956

Case	Fitted α / a.u.	MAE / J mol⁻¹	RMSE / J mol⁻¹	Max error / J mol⁻¹	R²
C5	313.628	0.25547	0.36189	0.60948	0.99999970

The explicit C5 generating equation, with energy in kJ mol⁻¹ and F in atomic units, is:

$$E_5(q,F) = 91.30(e^{-5.10u} - 2e^{-2.55u}) - 2625.49964[\frac{4.25}{2.541746473}e^{-0.75u}F + 155e^{-1.50u}F^2] - 5.00\times10^{-5}e^{-2.25u}(\frac{F}{10^{-4}})^4, \qquad u = q - 1. \qquad (89)$$

The corresponding fitted field equation at q = 1 is:

$$\hat{E}_5(x) = -91.30000 - 0.4390041881x - 0.004117154936x^2 \quad (\text{kJ mol}^{-1}). \quad (90)$$

Symmetric field sampling makes the odd and even columns of the regression matrix orthogonal. The linear coefficient therefore recovers the assigned dipole even when the quadratic approximation omits the fourth-order term. The quadratic column has a nonzero overlap with that omitted term and absorbs part of it, producing the positive polarisability bias in Eq. (86). This is a projection effect of the chosen model and field grid, rather than random variation in the assigned parameters.

The fitted C5 polarisability, 313.6283 a.u., is close to the geometry-relaxed value of 313.4775 a.u., but the two operations act on different energy curves. The former describes a quadratic fit at fixed q over a finite interval; the latter is a zero-field derivative after contact relaxation. The finite-difference estimate at h = 10^{-4} a.u., 313.8088 a.u., provides a third nearby number with a third origin. Agreement among such values must be interpreted through their definitions and limiting procedures.

Numerical convergence and fitting interval

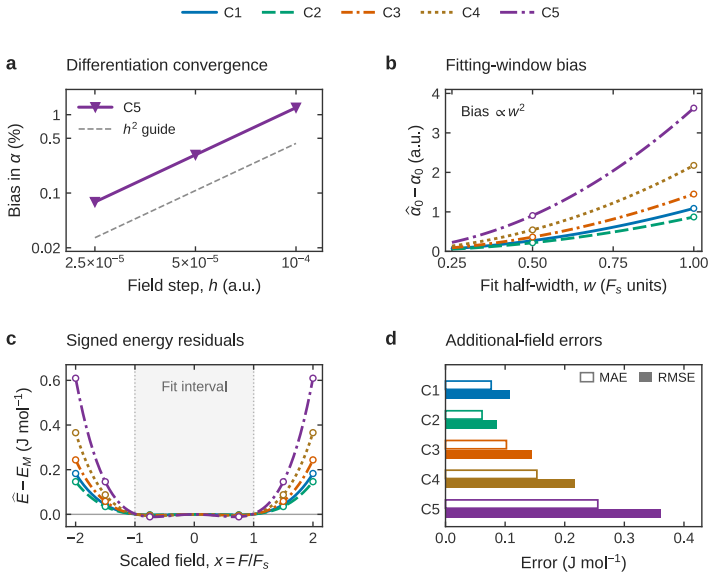


Figure 3. (a) C5 central-difference bias and h² guide. (b) Polarisability bias versus fit half-width w; the seven symmetric fields scale together. (c) Signed residuals, with the original fit interval shaded and additional checks marked by open circles. (d) Six-point MAE and RMSE. Colours follow Figure 1.

At zero field, Eq. (90) returns the assigned C5 minimum of −91.30 kJ mol⁻¹. At x = 1 it predicts a shift of −0.44312134 kJ mol⁻¹, close to the generating value of −0.44312371 kJ mol⁻¹. That agreement is expected within the sampled field range. Equation (88) identifies where the fit changes from slight underprediction to overprediction: the nonzero residual roots occur at the square root of ρ, approximately 0.976. The residual is negative inside those roots and positive at larger field magnitudes.

Scaling all seven training fields by a half-width w scales the ratio ρ by w^2. Figure 3b therefore shows that halving the window decreases the excess fitted polarisability by a factor of four. For C5, the bias falls from 3.6283 a.u. at w = 1 to 0.9071 a.u. at w = 0.5 and 0.2268 a.u. at w = 0.25. A smaller window better estimates the derivative at zero field; a wider window allocates more of the omitted nonlinearity to the fitted coefficient. The choice must follow the intended field range and observable.

Residual interpretation and transferability

The additional checks combine two points inside the fitting interval, x = ±0.75, with four outside it, x = ±1.50 and ±2.00. Their errors therefore probe both interpolation and extrapolation of the assigned function. For C5, the outermost magnitude produces the maximum absolute error of 0.60948 J mol⁻¹, whereas the six-point MAE and RMSE are 0.25547 and 0.36189 J mol⁻¹. The larger RMSE reflects the stronger weighting of the outer-field deviations. These metrics describe distinct features of the residual distribution.

The nearly unit R^2 values are dominated by recovery of the much larger dipolar energy variation. They consequently provide less information about the smaller even response than the coefficient bias and signed residuals. A model may recover the overall energy trend while assigning an inaccurate polarisability. Reporting errors in the energy, first derivative and second derivative separately, as anticipated by Eq. (49), makes that distinction explicit. The bars in Figure 3d compare deterministic metrics and do not represent replicate uncertainty.

For subsequent atomistic calibration, withholding nearby field points alone would leave the contact chemistry shared between training and assessment. Grouping parent structures, conformers and hydration classes instead tests the intended transfer between interfaces. The functional-form assessment of Hernandez & Mueller (2023) provides relevant context for evaluating analytical potentials beyond the configurations used to determine their parameters. Here the additional points test recovery of one assigned function; reference calculations on distinct contacts provide the next level of evidence.

Extended contact stationarity

A higher-order contact equation follows directly from the stationarity condition of Eq. (68). Set u = q − 1 and $x = F/F_s$, and expand the exponential terms about u = x = 0. The zero-field second, third and fourth contact derivatives are $k = 2Da^2$, $-6Da^3$ and $14Da^4$, respectively. Writing the stationary displacement as a power series and matching the coefficients of x, x^2 and x^3 gives the following extended expression. The atomic-unit dipole $\tilde{\mu}_0$ retains the conversion defined below Table 1.

$$0 = \frac{\partial E_M}{\partial u} = 2Da(e^{-au} - e^{-2au}) + K_E b\tilde{\mu}_0 F_s e^{-bu}x$$
$$+K_E b\alpha_0 F_s^2 e^{-2bu}x^2 + 3b\zeta e^{-3bu}x^4, \qquad x = F/F_s,$$
$$u_*(x) = -\frac{K_E b\tilde{\mu}_0 F_s}{2Da^2}x$$

$$+\left[\frac{K_E^2 b^2 \tilde{\mu}_0^2 F_S^2 (3a-2b)}{8D^2 a^4} - \frac{K_E b \alpha_0 F_S^2}{2Da^2}\right]x^2$$
$$+\frac{3K_E^2 b^2 \tilde{\mu}_0 \alpha_0 F_S^3 (a-b)}{4D^2 a^4} x^3$$
$$-\frac{K_E^3 b^3 \tilde{\mu}_0^3 F_S^3 (20a^2-27ab+9b^2)}{48D^3 a^6} x^3 + \mathcal{O}(x^4). \quad (91)$$

The first term in Eq. (91) is the linear response already obtained in Eq. (75). The quadratic term combines contact anharmonicity, the curvature of the dipole and the gradient of the clamped-coordinate polarisability. The cubic terms introduce higher derivatives and further cross-couplings, including the fourth derivative of the contact well. Their explicit dependence on D, a and b shows how a local contact shape controls nonlinear structural response. Because the derivative of the assigned quartic field term starts at x^4, ζ does not enter the displacement coefficients through x^3.

Fourth order stationary energy expansion

Substituting the stationary contact into the original potential yields an explicit relaxed-energy equation. To obtain terms through x^4, the displacement is required only through x^3: terms containing the next unknown displacement coefficient cancel because the leading stationarity condition is already satisfied. Combining the contact, dipolar and quadratic contributions then gives Eq. (92), including the fourth-order field coefficient ζ. The result uses the same energy units and assigned parameters as Eq. (68).

$$E_{\mathrm{rel}}(x) = E_M(1 + u_*(x), F_s x)$$
$$= -D + D(e^{-au_*} - 1)^2 - K_E \tilde{\mu}_0 F_s e^{-bu_*} x$$
$$-\frac{K_E \alpha_0 F_S^2}{2} e^{-2bu_*} x^2 - \zeta e^{-3bu_*} x^4$$
$$= -D - K_E \tilde{\mu}_0 F_s x - \frac{K_E F_S^2}{2}\left[\alpha_0 + \frac{K_E b^2 \tilde{\mu}_0^2}{2Da^2}\right]x^2$$
$$+F_S^3\left[\frac{K_E^3 b^3 \tilde{\mu}_0^3 (a-b)}{8D^2 a^4} - \frac{K_E^2 b^2 \tilde{\mu}_0 \alpha_0}{2Da^2}\right]x^3$$
$$-\left[\zeta + \frac{K_E^2 b^2 \alpha_0^2 F_S^4}{4Da^2}\right]x^4$$
$$+\frac{K_E^3 b^3 \tilde{\mu}_0^2 \alpha_0 F_S^4 (3a-4b)}{8D^2 a^4} x^4$$
$$-\frac{K_E^4 b^4 \tilde{\mu}_0^4 F_S^4 (a-b)(5a-4b)}{48D^3 a^6} x^4 + \mathcal{O}(x^5). \quad (92)$$

The quadratic coefficient in Eq. (92) reproduces Eq. (77), providing a consistency check between the second-order and extended derivations. A cubic energy term now appears even though the clamped-coordinate generating equation contains no cubic field term. It is created by eliminating the field-dependent contact coordinate. The fourth-order coefficient similarly contains both ζ and geometry-mediated contributions. Thus, the relaxed higher-order response cannot be obtained by transferring the clamped-coordinate coefficient without accounting for contact motion.

The C5 coefficients of x, x^2, x^3 and x^4 are −0.4390041881, −0.004115175276, $-1.6699284 \times 10^{-6}$ and $-5.0014620 \times 10^{-5}$ kJ mol^{-1}, respectively. At x = 1, full contact relaxation gives an energy shift of −443.17108 J mol^{-1}, or an additional lowering of 0.04737 J mol^{-1} relative to the clamped contact. Equation (92) differs from that relaxed value by only 3.17×10^{-5} J mol^{-1}. These values describe evaluation of the assigned analytical potential, consistent with the data statement above.

Verification of the extended equations

For C5, the coefficients multiplying x, x^2 and x^3 are $-2.7729931 \times 10^{-4}$, $-4.9046213 \times 10^{-6}$ and 7.4016718×10^{-9}. At x = 1, the full numerical contact shift is $-2.8229111 \times 10^{-4}$; the cubic approximation differs by 9.46×10^{-8}. Across $-2 \leq x \leq 2$, its maximum absolute displacement error is 1.52×10^{-6}. This residual is consistent with the first omitted fourth-order contribution and is examined independently in Figure 4a.

Figure 4 tests the truncation orders by comparing the explicit expressions with stationary contacts of the full exponential potential. On the positive-field branch, doubling x increases the cubic displacement error by approximately sixteenfold and the quartic energy error by approximately thirty-twofold. The x^4 and x^5 guides identify the first omitted powers rather than fitted performance targets. Independent polynomial composition also reproduces the coefficients of the expanded potential and cancels its gradient through x^3.

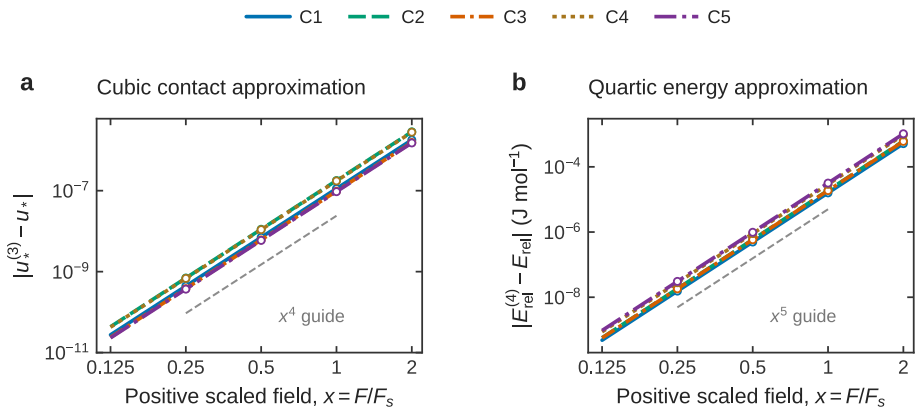


Figure 4. Errors of (a) the cubic contact approximation in Eq. (91) and (b) the quartic relaxed-energy approximation in Eq. (92), relative to numerical stationary contacts of the full potential. Open circles mark x = 0.25, 0.50, 1 and 2. The grey guides indicate the first omitted powers.

For C5 over $-2 \leq x \leq 2$, the maximum energy error decreases from 0.81463 J mol^{-1} for the second-order relaxed expansion to 0.001035 J mol^{-1} for Eq. (92), a reduction by about 787 times. Across all five cases, the maximum quartic energy errors range from 0.000515 to 0.001035 J mol^{-1}. These improvements concern truncation of the same generating function. The absolute remainder and the field range should accompany the order of an approximation when deciding whether the extra terms are useful.

The numerical checks establish algebraic consistency, a stable local expansion and reproducible recovery of the assigned contact response. An atomistic interfacial equation additionally needs reference energies and their derivatives for specified polymer conformers, zeolite sites and hydration environments. To enter an electronic self-consistent cycle, it must also define the density-dependent integrand and variational potential in Eqs. (52)–(54) and (66)–(67). The two extended equations provide analytical structure for that calibration while retaining a defined molecular coordinate and field domain.

CONCLUSION

A Lagrangian and variational framework was developed to describe poly(lactic acid)/polycaprolactone/poly(ethylene glycol) (PLA/PCL/PEG)–nanozeolite interfaces relevant to electric-field-assisted nonsolvent-induced phase separation (EFA-NIPS) under an applied voltage of 10 kV. The framework integrated molecular-level electromagnetic interactions, constrained electronic stationarity conditions, interfacial interaction energies, and electric-field derivatives to characterize the energy, electric dipole moment, polarizability, and geometry-relaxation response of a representative interfacial contact model. For the C5 polymer–zeolite configuration, which exhibited a minimum interaction energy of −91.30 kJ mol^{-1}, a nominal electric-field strength of 3.333×10^5 V m^{-1}, corresponding to an applied voltage of 10 kV across an assumed electrode separation of 3 cm, produced an energy shift of only −2.8459 J mol^{-1}, primarily attributable to dipole–field coupling. Geometric relaxation increased the calculated polarizability from 310.000 to 313.4775 atomic units (a.u.), demonstrating the contribution of structural relaxation to the interfacial electric-field response. However, reliable membrane-specific predictions will require calibration against converged atomistic density functional theory (DFT) reference calculations and independent validation using previously unexamined interfacial configurations and hydration environments. Further extension to a self-consistent density-functional framework will require incorporation of the explicitly derived variational potential and verification of numerical stability and convergence during self-consistent electronic-structure calculations.

FUNDING

This study did not receive any specific funding from governmental institutions, private organizations, or other funding agencies.

CONFLICT OF INTEREST

The authors declare that there are no conflicts of interest related to the conduct of the research, preparation, or publication of this article.

AUTHOR CONTRIBUTIONS

All authors contributed to the preparation of this article. Muhammad Satya Putra Gantada, Agung Mataram, was responsible for the conceptualization of the study, data collection and analysis, interpretation of the results, and manuscript preparation. The other authors contributed to the review, editing, and final approval of the manuscript.

GENERATIVE AI STATEMENT

The authors declare that no generative artificial intelligence was used in the preparation of this article.

REFERENCES

Cervellere, M. Rosario, Qian, Xianghong, Ford, David M., Carbrello, Christina, Giglia, Sal, & Millett, Paul C. (2021). Phase-field modeling of non-solvent induced phase separation (NIPS) for PES/NMP/Water with comparison to experiments. *Journal of Membrane Science*, *619*, 118779.

Colò, G., & Hagino, K. (2023). Orbital-free density functional theory: Differences and similarities between electronic and nuclear systems. Progress of Theoretical and Experimental Physics, 2023(10). https://doi.org/10.1093/ptep/ptad118

Damonte, G., Spotorno, R., Di Fonzo, D., & Monticelli, O. (2022). Multifunctional Porous Films Based on Polylactic Acid/Polycaprolactone Blend and Graphite Nanoplateles. ACS Applied Polymer Materials, 4(9), 6521–6530. https://doi.org/10.1021/acsapm.2c00923

Daub, C. D., & Kurtén, T. (2024). Effect of an Electric Field on the Structure and Stability of Atmospheric Clusters. The Journal of Physical Chemistry A, 128(3), 646–655. https://doi.org/10.1021/acs.jpca.3c07260

Gray, M., Bowling, P. E., & Herbert, J. M. (2022). Systematic Evaluation of Counterpoise Correction in Density Functional Theory. Journal of Chemical Theory and Computation, 18(11), 6742–6756. https://doi.org/10.1021/acs.jctc.2c00883

Gray, M., & Herbert, J. M. (2024). Assessing the domain-based local pair natural orbital (DLPNO) approximation for non-covalent interactions in sizable supramolecular complexes. The Journal of Chemical Physics, 161(5). https://doi.org/10.1063/5.0206533

Hernandez, A., & Mueller, T. (2023). Generalizability of functional forms for interatomic potential models discovered by symbolic regression. Physical Review Materials, 7(5), 053804. https://doi.org/10.1103/PhysRevMaterials.7.053804

Isidori, G., Wilsch, F., & Wyler, D. (2024). The standard model effective field theory at work. Reviews of Modern Physics, 96(1), 015006. https://doi.org/10.1103/RevModPhys.96.015006

Kirkpatrick, J., McMorrow, B., Turban, D. H. P., Gaunt, A. L., Spencer, J. S., Matthews, A. G. D. G., Obika, A., Thiry, L., Fortunato, M., Pfau, D., Castellanos, L. R., Petersen, S., Nelson, A. W. R., Kohli, P., Mori-Sánchez, P., Hassabis, D., & Cohen, A. J. (2021). Pushing the frontiers of density functionals by solving the fractional electron problem. Science, 374(6573), 1385–1389. https://doi.org/10.1126/science.abj6511

Kurniawan, R. A., & Chu, P. P.-J. (2024). The effect of electric field-assisted non-solvent induced phase separation method on PVDF membrane morphologies and performances. Polymer-Plastics Technology and Materials, 63(6), 703–715. https://doi.org/10.1080/25740881.2024.2302538

Li, L. (2021). Comprehensive investigations of interaction properties of polylactic Acid–Attapulgite composite by reactive molecular dynamics simulations and dispersion corrected DFT calculations. Current Applied Physics, 28, 78–86. https://doi.org/10.1016/j.cap.2021.05.001

Manholi, S., & Athiyanathil, S. (2022). Poly (ε-caprolactone)-based porous membranes for filtration applications—effect of solvents on precipitation kinetics, performance, and morphology. Journal of Applied Polymer Science, 139(10). https://doi.org/10.1002/app.51720

Neese, F. (2022). Software update: The ORCA program system—Version 5.0. WIREs Computational Molecular Science, 12(5). https://doi.org/10.1002/wcms.1606

Stanciakova, K., Louwen, J. N., Weckhuysen, B. M., Bulo, R. E., & Göltl, F. (2021). Understanding Water–Zeolite Interactions: On the Accuracy of Density Functionals. The Journal of Physical Chemistry C, 125(37), 20261–20274. https://doi.org/10.1021/acs.jpcc.1c04270

Wang, P., Gao, S., Chen, X., Yang, L., Cao, T., Fan, B., Liu, J., & Hu, X. (2022). Effect of PCL-b-PEG Oligomer Containing Ionic Elements on Phase Interfacial Properties and Aggregated Structure of PLA/PCL Blends. Macromolecular Research, 30(7), 438–445. https://doi.org/10.1007/s13233-022-0058-0

Zhang, H., Liu, S., You, J., Liu, C., Zheng, S., Lu, Z., Wang, T., Zheng, N., & Shao, B. (2024). Overcoming the barrier of orbital-free density functional theory for molecular systems using deep learning. Nature Computational Science, 4(3), 210–223. https://doi.org/10.1038/s43588-024-00605-8